RSC Advances

PAPER

View Article Online
View Journal | View Issue

Cite this: *RSC Adv.*, 2022, **12**, 1278

High performance and gate-controlled $GeSe/HfS_2$ negative differential resistance device†

Amir Muhammad Afzal, *[a] Muhammad Zahir Iqbal,[b] Muhammad Waqas Iqbal,[a] Thamer Alomayri,[c] Ghulam Dastgeer,[d] Yasir Javed,[e] Naveed Akhter Shad,[f] Rajwali Khan,[g] M. Munir Sajid,[f] R. Neffati,[hi] Tasawar Abbas[a] and Qudrat Ullah Khan[j]

Received 29th September 2021
Accepted 6th December 2021

DOI: 10.1039/d1ra07276e

rsc.li/rsc-advances

Transition metal dichalcogenides (TMDs) have received significant attention owing to their thickness-dependent folded current–voltage (I_{ds}–V_{ds}) characteristics, which offer various threshold voltage values. Owing to these astonishing characteristics, TMDs based negative differential resistance (NDR) devices are preferred for the realization of multi-valued logic applications. In this study, an innovative and ground-breaking germanium selenide/hafnium disulfide (p-GeSe/n-HfS_2) TMDs van der Waals heterostructure (vdWH) NDR device is designed. An extraordinary peak-to-valley current ratio (≈5.8) was estimated at room temperature and was used to explain the tunneling and diffusion currents by using the tunneling mechanism. In addition, the p-GeSe/n-HfS_2 vdWH diode was used as a ternary inverter. The TMD vdWH diode, which can exhibit different band alignments, is a step forward on the road to developing high-performance multifunctional devices in electronics.

Introduction

Graphene (Gr), formed from a single layer of carbon atoms, is considered to be a suitable material for use in field-effect transistors (FETs), photodetectors and sensors owing to its zero bandgap.[1–4] The zero bandgap in Gr has inspired researchers to develop a novel family of materials that possess a suitable bandgap and have analogous features.[5,6] Beyond the discovery of Gr,[7] the transition metal dichalcogenides (TMDs) are considered to possess remarkable high performance electronic and optoelectronic characteristics.[8] TMDs based devices are widely used in different applications, such as photovoltaics, data storage, diodes, and as chemical sensors.[9–13]

Black phosphorus (BP) and molybdenum ditelluride ($MoTe_2$) have been widely used in high-performance devices because of their thickness-dependent bandgap and work function, large hole charge carrier densities, and unexpected mobility. Recently, both materials have attracted extraordinary attention owing to their unique optical characteristics.[14–16] On the other hand, the electronic and optical properties show deterioration because both TMDs are unstable and easily oxidized under ambient conditions.[17] In contrast, GeSe, an emerging and auspicious p-type transition metal dichalcogenide (TMD), with a unique structure, is considered to be an alternate to BP. The bandgap nature of GeSe changes from indirect (1.08 eV) to direct (1.7 eV) in the bulk compared to the monolayer, respectively.[18–20] It has significant application potential in FETs, chemical sensors, and photovoltaic devices.[21]

Other widely studied Hf-based layered TMDs, such as HfS_2 and $HfSe_2$, in which the layers are linked by van der Waals forces, have been discovered. The HfS_2 has an octahedral coordinate structure with an indirect bandgap (1.1–1.2 eV) in the case of the monolayer.[22] It has broad applications in electronics and optoelectronics because of its narrow bandgap, large and tunable work function, and huge mobility.[23–25] It is clear from the literature that the device applications of HfS_2 are quite limited. Contact resistance also plays a vital role in the performance of the devices; a genuine issue is presented when the work function is not the same as that of the TMDs materials and metal contacts.[26,27] If there is contact resistance between the

[a]*Department of Physics, Riphah International University, 13 Raiwind Road, Lahore, Pakistan. E-mail: amirafzal461@gmail.com*
[b]*Nanotechnology Research Laboratory, Faculty of Engineering Sciences, GIK Institute of Engineering Sciences and Technology, Topi 23640, Khyber Pakhtunkhwa, Pakistan*
[c]*Department of Physics, Faculty of Applied Science, Umm-Al-Qura University, 21955, Makkah, Saudi Arabia*
[d]*Department of Physics & Astronomy, Graphene Research Institute–Texas Photonics Center International Research Center (GRI–TPC IRC), Sejong University, Seoul 05006, Korea*
[e]*Department of Physics, University of Agriculture, Faisalabad, 38000, Pakistan*
[f]*Department of Physics, GC University, Faisalabad, 38000, Pakistan*
[g]*Department of Physics, University of Lakki Marwat, Lakki Marwat, KPK, Pakistan*
[h]*Department of Physics, Faculty of Science, King Khalid University, P.O. Box 9004, Abha, Saudi Arabia*
[i]*Laboratoire de Physique de la Matière Condensée, Département de Physique, Faculté des Sciences de Tunis, Université Tunis El Manar, Campus Universitaire, 1060 Tunis, Tunisia*
[j]*Greater Bay Area Institute of Precision Medicine (Guangzhou), Fudan University, Nansha District, Guangzhou, Guangdong 511458, P. R. China*

† Electronic supplementary information (ESI) available. See DOI: 10.1039/d1ra07276e

metal contact and the TMDs materials it is difficult to achieve a high performance in electronics and optoelectronics. By stacking the TMDs materials, a compact system is developed called the van der Waals heterostructures (vdWHs), which offers a novel platform to develop nano-devices.

The nano devices based on 2D-TMDs vdWHs have been efficiently used in FETs,[28] sensors,[29] data storage devices,[30] photodetectors,[31–34] integrated circuits,[35] energy storage,[36] amplifiers,[37] inverters,[38] spin-field effect transistors,[39] water splitting,[40] and diodes.[38,41] Heterostructures and homojunction type devices have been designed by the doping of TMDs materials (chemically and electrostatically), and Fermi-level pinning. These techniques are not suitable for use in a high-performance device. The performance of the devices decreased with the passing of time. Secondly, the performance of the TMDs based nano devices is also controlled by controlling the Schottky barrier height (ϕ_B) of the metal–TMDs junction.[38,42] The ϕ_B is considered to be a key parameter to control the performance of nano devices.

Hence, the 2D-TMDs vdWHs multifunctional devices with extraordinary performances, such as negative differential resistance (NDR) diode type devices and a high value of peak-to-valley current ratio, have yet to be realized. In this research, we fabricated advanced and unique GeSe/HfS_2 vdWHs for multiple applications, such as NDR diode type devices and broadband photo-detecting. Each material (p-GeSe and n-HfS_2) was characterized using different metal contacts to estimate the low resistance electrode and high mobility. The high peak-to-valley current ratio values were estimated at room temperature and explain the tunneling and diffusion currents using the tunneling mechanism. These high gate-modulated NDR characteristics, with an extraordinary peak-to-valley current, represent an outstanding potential in electronics, which are likely to be essential when developing highly efficient multi-valued logic applications.

Materials and methods

Device fabrication

Nano-flakes of the TMDs material (p-GeSe and n-HfS_2) were obtained by mechanical exfoliation. The Scotch tape method was used to exfoliate the materials. The dry transfer method was used to fabricate the NDR devices. A compound microscope was used to observe and estimate the thickness of the p-GeSe flakes. After selection of the GeSe flake, a polydimethylsiloxane (PDMS) stamp was used to make the n-HfS_2 flake a suitable size and it was then placed onto a p-GeSe flake with a micro-aligner stage. The electrode pattern was designed, and a thermal evaporation system was used for the metal contacts of (Pd/Au, Ni/Au, Cr/Au, and Ag/Au: 6/60 nm) and (Sc/Au, Al/Au, Ti/Au, Pt/Au: 6/60 nm) for p-GeSe and n-HfS_2, respectively. For the lift-off process, acetone was used.

All of the measurements (electrical) were performed in a vacuum box with a Keithley-2400 and Keithley-6485.

Results and discussion

The p-type GeSe was exfoliated and moved onto the substrate (p-Si/SiO_2 = 300 nm) with the help of a micro-aligner attached to the camera of a microscope. The n-type HfS_2 was transferred onto the GeSe to form the vdWHs. A schematic diagram is shown Fig. 1a. The optical image of the final device is shown in Fig. 1b. Raman spectroscopy was used for the identification of materials. Fig. 1c shows the Raman spectra of each material (GeSe and HfS_2) and the heterostructure. Raman spectroscopy was used to determine the nature of the materials. Fig. 1c shows the Raman spectra of GeSe, HfS_2, and GeSe/HfS_2. The peaks that appear at 151.8 and 191 cm^{-1} in the case of GeSe match those observed in the previously published literature.[19,43] In the case of n-HfS_2, the Raman peaks appeared at 260 and 337 cm^{-1} and the Raman modes are consistent with previous reports.[44,45]

Atomic force microscopy (AFM) was used to determine the thickness of the p-GeSe and n-HfS_2 flakes, and these were found to lie in the range of 16 and 28 nm, respectively. The AFM image with height profiles is shown in Fig. S1a and b (ESI†). The electrode Pd/Au and Sc/Au is used for p-GeSe and HfS_2, respectively, to form the low resistance contacts. The types of charge carriers in p-GeSe and n-HfS_2 were confirmed by the transfer curve at a constant V_{ds} = 0.5 V (Fig. S2a and b†). The V_{bg} was swept between ±40 V and measured the output across the source to the drain.

First, we measured the p-GeSe and n-HfS_2 field-effect transistors with dissimilar metal electrodes and then performed electrical measurements. To estimate the electrical performance, the charge carrier mobility (μ_{FE}) of p-GeSe and n-HfS_2 was measured. The μ_{FE} of the device was extracted by using the following relationship:[46]

$$\mu_{FE} = \frac{L}{W}\left(\frac{dI_{ds}}{dV_{bg}}\right)\frac{1}{C_{bg}V_{ds}} \quad (1)$$

In which, L and W represent the length and width of the channel respectively, $\left(\frac{dI_{ds}}{dV_{bg}}\right)$ provides the slopes, and C_{bg} is the gate capacitance. In GeSe FET, the estimated μ_{FE} were observed to be Pd = 90.7, Ni = 74.5, Cr = 51.4, and Ag = 43.5 $cm^2\ V^{-1}\ s^{-1}$.[47] Secondly, the conceived μ_{FE} in the case of n-HfS_2 with Sc, Al, Ti, and Pt were found to be 75, 61.6, 42.5, and 36 $cm^2\ V^{-1}\ s^{-1}$ (Fig. 1d). In the case of the ohmic contacts (Pd–GeSe/Sc–HfS_2), a large hole/electron mobility and lower value of the threshold voltage were obtained because of the high/low work function, respectively. The Pd/Sc metals with a high/low work function doped the GeSe/HfS_2 TMDs materials and improved the charge carrier densities in the channel of the device. Furthermore, the current–voltage (I_{ds}–V_{ds}) characteristics were estimated using various contacts to determine the linear and non-linear behavior of the electrodes. Fig. S3† displays the I_{ds}–V_{ds} curves of the GeSe and HfS_2 with various metal contacts. The metal contact (Pd), which has a high work function, shows a linear behavior (ohmic) with GeSe. Other metals show non-linear curves because of the difference in the work function. The

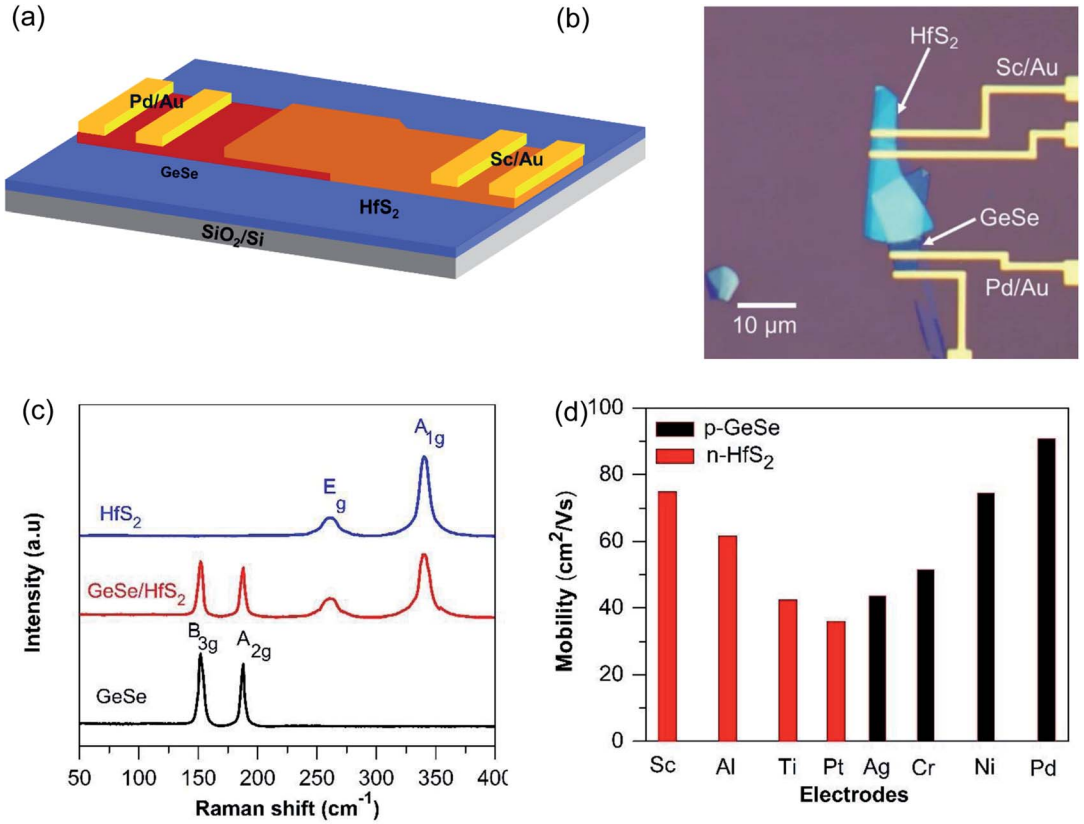

Fig. 1 (a) Schematic diagram of the GeSe/HfS_2 broken band gap p–n heterojunction device. (b) Optical image of the p-GeSe/n-HfS_2 broken band gap p–n junction. (c) Raman spectroscopy of each flake (GeSe and HfS_2) and the heterojunction (GeSe/HfS_2) device, respectively. (d) Mobility of the p-GeSe and HfS_2 TMDs with different electrodes.

linear behavior of the I_{ds}–V_{ds} curves validate the ohmic behavior because of the low potential barrier between the junction of the metal–TMDs. Furthermore, the I_{ds}–V_{ds} characteristics were also measured with different electrodes (Sc, Al, Ti, and Pt) to find the most suitable electrode for high-performance n-HfS_2 devices. Primarily, the linear tendency of the I_{ds}–V_{ds} characteristics depends on the difference in the work function between the metal and TMDs materials and potential barrier between them. The energy band diagram of the GeSe with different metals before and after contact between the metals and the GeSe material is shown in Fig. S4.† The values of the work functions, electron affinities and bandgaps of GeSe and n-HfS_2 were taken from previously reported studies.[41,48–56]

Temperature-dependent electrical measurements were performed to obtain the Schottky barrier height (ϕ_B). Then, we extracted the ϕ_B between the metals with TMDs by using the standard current model for thermionic emission, given as:

$$I_{ds} = AA^{*}T^{2}\exp\left(\frac{-q\phi_B}{k_BT}\right)\left[\exp\left(\frac{qV}{k_BT}\right) - 1\right], \quad (2)$$

In which, A is the area of the junction, A^* is the Richardson constant, q is the elementary charge (1.6×10^{-19} C), k_B is the Boltzmann's constant (1.38×10^{-23} m^2 kg s^{-2} K^{-1}), and T is the temperature, respectively. Fig. S5† shows the $\ln\left(\frac{I}{T^2}\right)$ plotted against $\frac{q}{k_BT}$, which is used for the estimation of the ϕ_B height at metal–TMD junctions. The estimated values of ϕ_B are 29, 45, 58, and 68 meV for Pd, Ni, Cr, and Ag, respectively. In the case of HfS_2, the obtained values of ϕ_B are 41, 52, 60, and 78 meV for Sc, Al, Ti, and Pt, respectively. After the optimization of the most suitable electrode for the Pd–GeSe/Sc–HfS_2 vdWH heterojunction device, the NDR characteristics were measured. After successfully designing the GeSe/HfS_2 TMDs vdWH NDR device, the electrical measurement was performed at room temperature. Fig. 2a shows the current–voltage values (I_{ds}–V_{ds}) are measured at zero back gate voltages (V_{bg}). The device demonstrates a high value for the peak-to-valley current ratio (PVCR = 5.4) between 0.5 V and 1.1 V, which is larger than the previously reported literature values.[57,58] The highest and lowest values of the current are called the peak current (I_{peak}) and the valley current (I_{valley}). Fig. 2b shows the gate-dependent I_{ds}–V_{ds} characteristics, which indicates that the peak current (I_{peak}) is successfully modulated using the back gate voltage (V_{bg}). When the V_{bg} decreases, the I_{peak} also decreases. When the V_{bg} is tuned from 40 V to −40 V, the Fermi level (E_f) of GeSe moves downward because of the accumulation of charge carriers (holes).[59]

As a result, the energy band bending of GeSe is increased. The E_f of HfS_2 is hardly tuned by V_{bg} because of the thick GeSe. The shifting of the energy band in the downward direction in

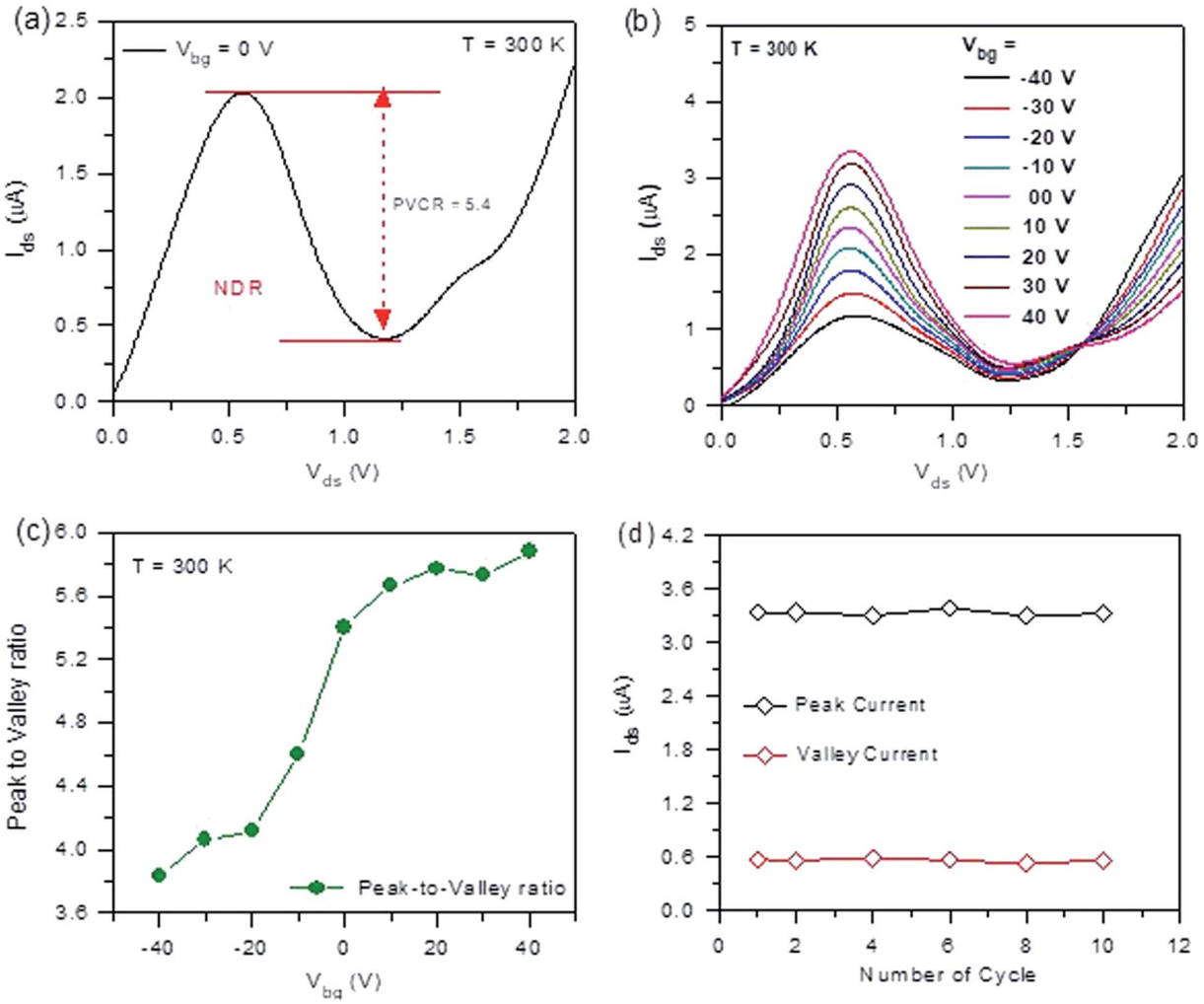

Fig. 2 Electrical measurement of the p-GeSe/n-HfS_2 NDR devices. (a) Current as a function of the bias voltage at $V_{bg} = 0$ V. (b) Change in current at different V_{bg} of p-GeSe/n-HfS_2 NDR devices. (c) Change in the peak to the valley with back gate voltage at room temperature. (d) Change in the peak current and valley current *versus* the number of cycles.

GeSe behaves like a potential well at the interface of the heterojunction, which decreases the I_{peak}. It is difficult to escape the charge carriers from the potential well because of the strong confinement of the electron carriers in the potential well. Therefore, the value of PVCR for the heterojunction was tuned to between 3.83 and 5.87 A/A using the V_{bg} (−40 V to 40 V) (Fig. 2c). To check the stability of the I_{peak} to I_{valley}, ten consecutive I_{ds}–V_{ds} sweeps were measured. The estimated values show stable peak- and valley-current values (Fig. 2d).[60]

For a graphical explanation of the NDR mechanism, a band energy diagram is shown in Fig. 3. Fig. 3a shows the band energy diagram of the GeSe/HfS_2 TMDs vdWH NDR device before and after contact at a zero biased voltage. The $E_f$of the GeSe and HfS_2 are aligned after contact at the same level. A type-III bandgap (broken bandgap) was developed between the GeSe and HfS_2 because the valence band of the GeSe exists above the conduction band of HfS_2. The current mechanism can be explained based on the diffusion and tunneling current by using the band energy diagram. Fig. 3b shows the energy band diagram of the GeSe/HfS_2 TMDs vdWH NDR device under a different bias voltage. At a negative bias voltage ($V_{ds} < 0$ V), the tunneling current becomes prominent over the diffusion current. During the negative region, the charge carriers (electron) tunnel from GeSe (filled valence band states) to HfS_2 (empty conduction band states), which amplifies the current. The tunneling current also becomes prominent between 0 and 0.5 V. In this region, the charge carriers (electrons) tunnel from the conduction band of HfS_2 to the empty valence states of GeSe, increasing the current. The current is unceasingly enhanced in anticipation of the Fermi level of HfS_2, which is aligned with the uppermost valence band energy of the GeSe. The overlapping of the filled states in HfS_2 with unoccupied states in GeSe gives rise to the maximum tunneling current (I_{peak}). In the range of 0.5 V < V_{ds} < 1 V, the magnitude of the current is decreased because of the reduction in the degree of overlap between the filled and empty states. Therefore, the tunneling current is decreased as the V_{bias} is increased, which results from the NDR behavior in the heterojunction device. At a higher bias voltage (V_{ds} > 0.5 V), the diffusion current predominantly contributes to the NDR behavior of the GeSe/

HfS_2 TMDs vdWH NDR device. In this region, the electrons are capable of diffusing from HfS_2 to GeSe by attenuating the potential well, which again increases the current in the device.

Furthermore, to check the effect of temperature, the I_{ds}–V_{ds} measurements were performed at different temperatures from 50–300 K (Fig. 4a). We observed that the I_{peak} is improved, whereas the I_{valley} declined with the falling temperature (Fig. 4b and c). The value of the peak-to-valley current was enhanced from 5.8 to 10 A/A with the temperature (Fig. 4d). The values of the peak voltage and valley voltage were shifted towards positive values. To confirm the highest values (Table S1†) of the peak and valley current, the analytic NDR device model was used. The I_{ds}–V_{ds} characteristics were also measured using this model and the peak-to-valley ratio was estimated. The total current (tunneling and diffusion current) is calculated by using the following equation:[52]

$$I_{tunnel} = \frac{2\pi\alpha q}{h}\int_{E_c-HfS_2}^{E_v-GeSe} DOS_{GeSe}(E)\times DOS_{HfS_2}(E)\times\left[f_{GeSe}(E) - f_{HfS_2}(E-q(V-IR_s))\right]\times dE \quad (3)$$

$$I_{diff} = qI_0\left[\exp\left(\frac{V-IR_s}{\eta_{id}k_BT}\right)-1\right] \quad (4)$$

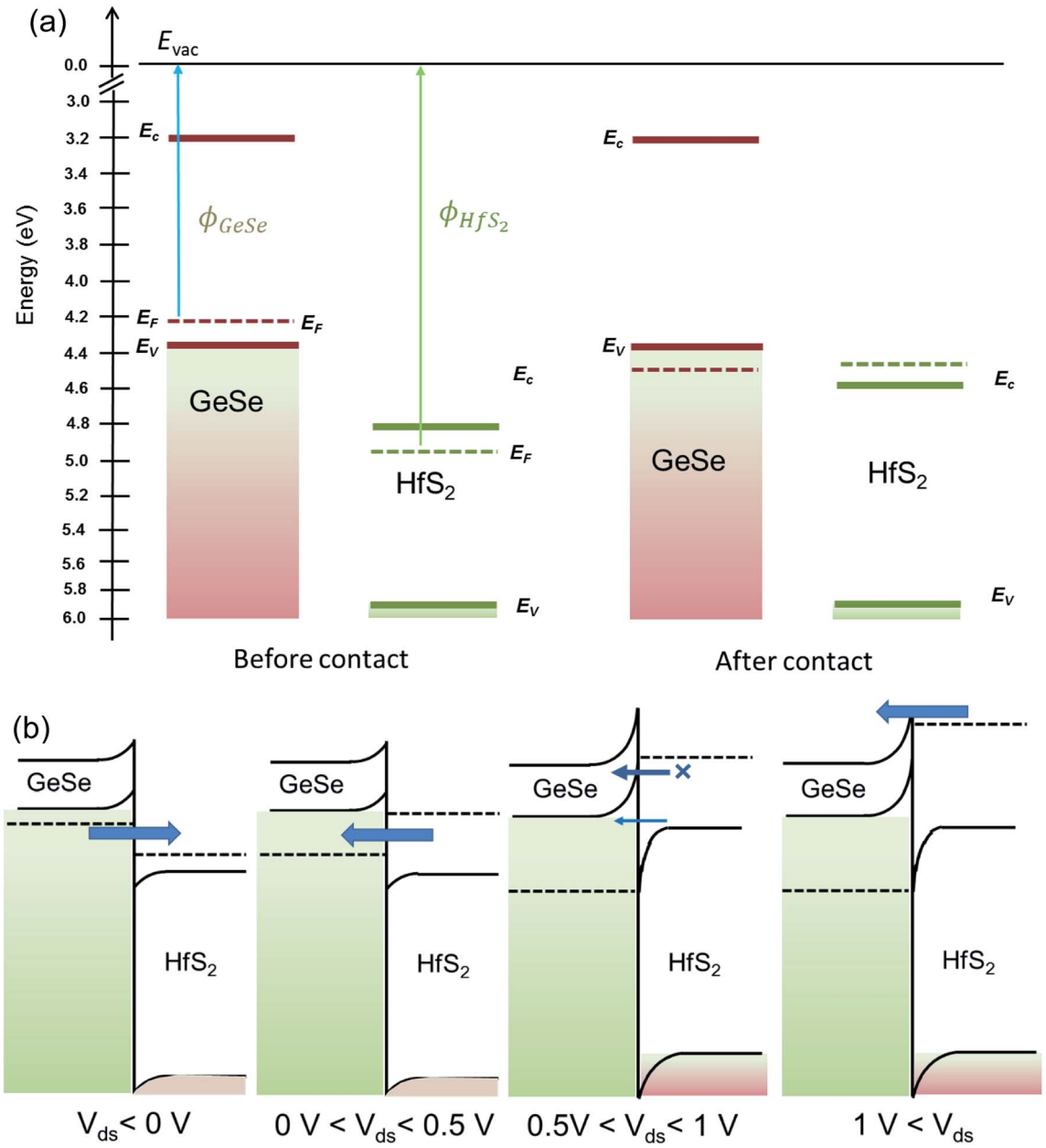

Fig. 3 (a) Energy band diagram of the p-GeSe/n-HfS_2 NDR heterojunction device before contact and after contact at zero back gate voltage. (b) Energy band diagram of the p-GeSe/n-HfS_2 NDR device at different V_{ds}.

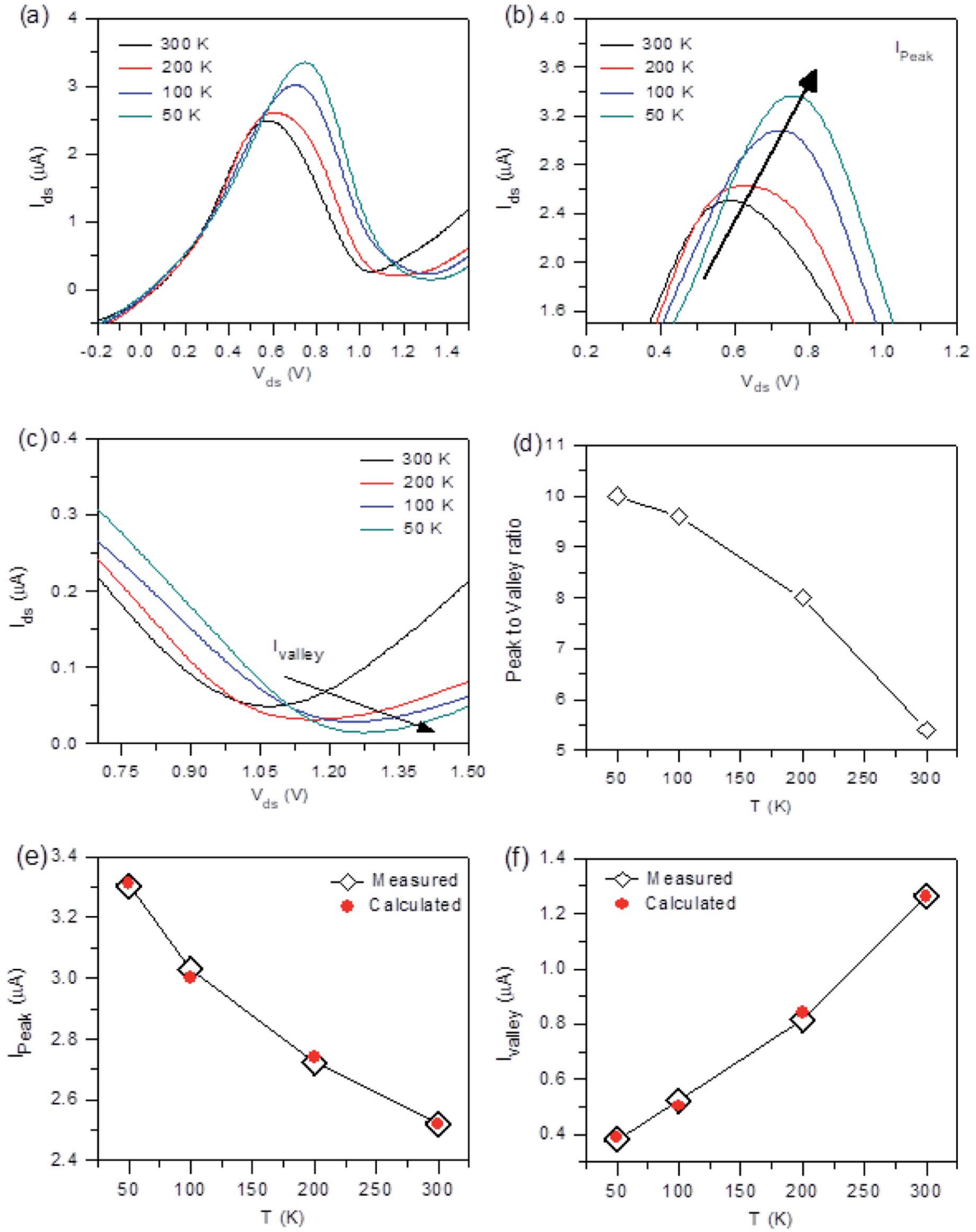

Fig. 4 (a) Current–voltage (I_{ds}–V_{ds}) characteristics of the GeSe/HfS_2 NDR device at different temperatures. (b) Change in the valley current with the temperature. (c) Change in the valley current with the temperature of the GeSe/HfS_2 NDR devices. (d) Change in the peak to valley current with temperature of the GeSe/HfS_2 NDR devices. (e) Comparison of the measured and calculated value of the peak current as a function of time. (f) Comparison of the measured and calculated value of the valley current as a function of time.

In which α, E_v – GeSe, E_c – HfS_2, $DOS_{GeSe}(E)$, $DOS_{HfS_2}(E)$, $f_{GeSe}(E)$, and $f_{HfS_2}(E)$ represents the screening factor, the highest valence band energy in GeSe, the lowest conduction band energy in HfS_2, the density of states and the Fermi–Dirac distribution functions of GeSe and HfS_2, respectively. Fig. 4e and f show the measured and calculated values, which demonstrate the consistency of the results. The measured value is obtained from the experimental data. The calculated value is

conceived from the theoretical I_{ds}–V_{ds} curves estimated using the analytical model.

Basically, most of the I_{peak} is primarily occupied by tunnel currents. The I_{peak} looks to be allied with the density of states in the CB and VB of the HfS_2 and GeSe. Both the current values (I_{peak} and I_{valley}) show different behaviors because the tunneling current is increased and the diffusion current is decreased as the temperature decreases. The parasitic series resistance (R_s) was also determined using the analytic model to enable accurate analysis. The R_s is the contact resistance between the contact and TMD materials. The metal–semiconductor (MS) junction resistance is enhanced at a lower temperature because of the decline in the n-type charge carriers, which leads to an enhanced depletion width at the MS junction. Therefore, a high voltage value is required to operate the NDR device at a lower temperature.[61,62] We measured multiple devices of the same thickness to check the self-consistency (Fig. S6†). The effect of the thickness is also measured, as shown in Fig. S8.† In the case of a few layers, the device shows a linear behavior because of direct tunneling. Finally, an innovative ternary inverter has been designed, which is the elementary building block of multivalued logic applications. This ternary inverter is fabricated by using the GeSe/HfS_2 TMDs vdWH. In most thin-film transistors (TFT), the BP was used as p-channel materials that oxidize in the ambient environment and decrease the performance of the devices.[52]

To overcome this critical issue, we used p-GeSe as a p-channel material. The entire resistance (R) in GeSe could be controlled by V_{bg}. The source and back gate electrodes were used as a supply and input voltage, respectively. The electrode on HfS_2 is connected to the ground. The output voltage is measured across the middle-shared electrode. Fig. 5d shows the change in V_{OUT} as a function of V_{IN} at fixed $V_{DD} = 2$ V from 5 to 25 V. We observed three distinct states that are mentioned as state-2, state-1, and state-0. At state 2, the output voltage is greater than 1.75 V, which appears at 4.9 V< V_{Input} < 7.9 V. In state-1 and 0 the output voltage is around 0.85 and 0.22 V, respectively (Fig. 5d). Load line circuit analysis was performed to explain the working of the inverter. The point of intersection

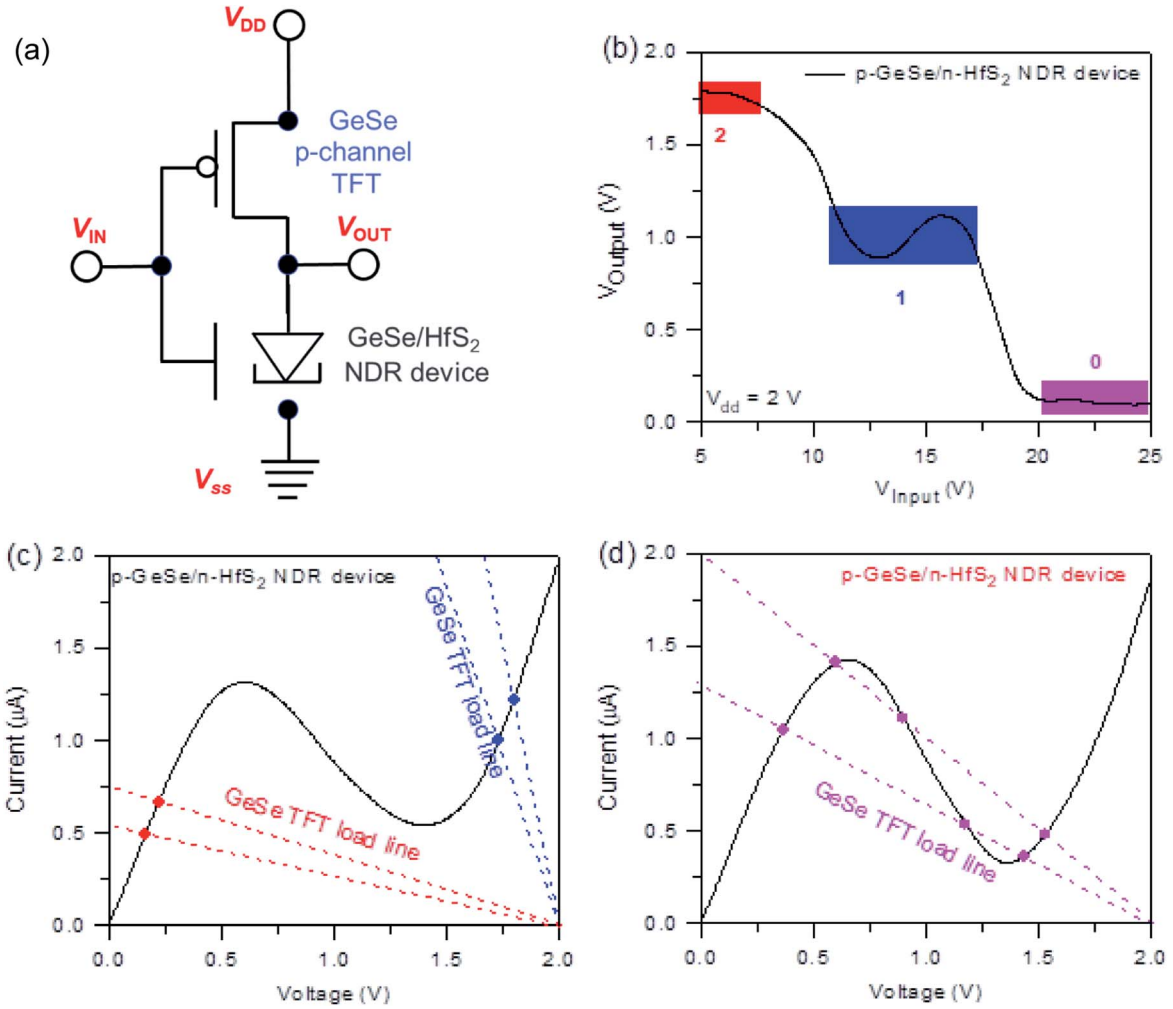

Fig. 5 Ternary inverter (p-GeSe/n-HfS_2 NDR) device: (a) an analog circuit representation of the ternary inverter p-GeSe/n-HfS_2 NDR device. (b) Output *versus* input characteristics of the ternary inverter p-GeSe/n-HfS_2 NDR device. (c and d) Load line analysis under different bias conductions for the GeSe/HfS_2 ternary inverter device.

between the two curves indicates the point of operation of the circuit (Fig. 5c and d).

During the low voltage range, the load resistor offers a path with a small resistance between the source and drain. In this state, the input voltage is higher than the threshold voltage and a high value of the output voltage is obtained, which is almost equal to the V_{DD}. When a high voltage is applied at the input terminal, the GeSe TFT is turned off and the resistance decreases between the output terminal and the ground. At an intermediate voltage, the device works as an NDR device. The ternary device based on GeSe/HfS_2 TMDs provides an opportunity to develop multi-valued logic applications.

Conclusion

In this work, we designed a novel and innovative p-GeSe/n-HfS_2 TMDs vdWH diode type NDR device. An astonishing peak-to-valley current ratio ($\approx$5.8) was conceived at 300 K. The NDR device was also measured at different back-gate voltages and the NDR behavior was successfully modulated. The performance of the NDR device was also measured at different temperatures. From an application point of view, the p-GeSe/n-HfS_2 vdWH) diode was used as a ternary inverter.

Conflicts of interest

The authors declare no conflicts of interest.

Author contributions

A. M. Afzal performed the experimental work and wrote the manuscript. M. Z. Iqbal, M. W. Iqbal, T. Alomayri, G. Dastgeer, Y. Javed, N. A. Shad, R. Khan, M. M. Sajid, R. Neffati, T. Abbas, and Q. U. Khan helped with the experimental work.

Acknowledgements

The author (R. Neffati) extends his appreciation to the Deanship of Scientific Research at King Khalid University, Saudi Arabia for funding this work through the Research Groups Program under grant number (R.G.P.2/170/42).

References

1 A. K. Geim and K. S. Novoselov, in *Nanoscience and Technology: A Collection of Reviews from Nature Journals*, World Scientific, 2010, pp. 11–19.
2 E. P. Randviir, D. A. Brownson and C. E. Banks, *Mater. Today*, 2014, **17**, 426–432.
3 Y. Zhang, Y.-W. Tan, H. L. Stormer and P. Kim, *Nature*, 2005, **438**, 201.
4 K. S. Novoselov, A. K. Geim, S. V. Morozov, D. Jiang, Y. Zhang, S. V. Dubonos, I. V. Grigorieva and A. A. Firsov, *Science*, 2004, **306**, 666–669.
5 K. F. Mak, C. Lee, J. Hone, J. Shan and T. F. Heinz, *Phys. Rev. Lett.*, 2010, **105**, 136805.
6 M. Chhowalla, H. S. Shin, G. Eda, L.-J. Li, K. P. Loh and H. Zhang, *Nat. Chem.*, 2013, **5**, 263.
7 G. R. Bhimanapati, Z. Lin, V. Meunier, Y. Jung, J. Cha, S. Das, D. Xiao, Y. Son, M. S. Strano and V. R. Cooper, *ACS Nano*, 2015, **9**, 11509–11539.
8 P. Johari and V. B. Shenoy, *ACS Nano*, 2012, **6**, 5449–5456.
9 H. Wang, H. Feng and J. Li, *Small*, 2014, **10**, 2165–2181.
10 Y. Zhang, B. Zheng, C. Zhu, X. Zhang, C. Tan, H. Li, B. Chen, J. Yang, J. Chen and Y. Huang, *Adv. Mater.*, 2015, **27**, 935–939.
11 K. F. Mak and J. Shan, *Nat. Photonics*, 2016, **10**, 216.
12 B. W. Baugher, H. O. Churchill, Y. Yang and P. Jarillo-Herrero, *Nat. Nanotechnol.*, 2014, **9**, 262.
13 M.-L. Tsai, S.-H. Su, J.-K. Chang, D.-S. Tsai, C.-H. Chen, C.-I. Wu, L.-J. Li, L.-J. Chen and J.-H. He, *ACS Nano*, 2014, **8**, 8317–8322.
14 I. G. Lezama, A. Arora, A. Ubaldini, C. Barreteau, E. Giannini, M. Potemski and A. F. Morpurgo, *Nano Lett.*, 2015, **15**, 2336–2342.
15 C. Ruppert, O. B. Aslan and T. F. Heinz, *Nano Lett.*, 2014, **14**, 6231–6236.
16 I. G. Lezama, A. Ubaldini, M. Longobardi, E. Giannini, C. Renner, A. B. Kuzmenko and A. F. Morpurgo, *2D Mater.*, 2014, **1**, 021002.
17 J. S. Ross, P. Klement, A. M. Jones, N. J. Ghimire, J. Yan, D. Mandrus, T. Taniguchi, K. Watanabe, K. Kitamura and W. Yao, *Nat. Nanotechnol.*, 2014, **9**, 268.
18 M. Koike, E. Shikoh, Y. Ando, T. Shinjo, S. Yamada, K. Hamaya and M. Shiraishi, *Appl. Phys. Express*, 2013, **6**(2), 023001.
19 H. Zhao, Y. Mao, X. Mao, X. Shi, C. Xu, C. Wang, S. Zhang and D. Zhou, *Adv. Funct. Mater.*, 2018, **28**, 1704855.
20 A. M. Afzal, M. Z. Iqbal, S. Mumtaz and I. Akhtar, *J. Mater. Chem. C*, 2020, **8**, 4743–4753.
21 S. H. Jo, H. W. Lee, J. Shim, K. Heo, M. Kim, Y. J. Song and J. H. Park, *Adv. Sci.*, 2018, **5**, 1700423.
22 W. Zhang, Z. Huang, W. Zhang and Y. Li, *Nano Res.*, 2014, **7**, 1731–1737.
23 C. Lei, Y. Ma, X. Xu, T. Zhang, B. Huang and Y. J. T. Dai, *J. Phys. Chem. C*, 2019, **123**, 23089–23095.
24 J. Chang, *J. Appl. Phys.*, 2015, **117**, 214502.
25 C. Gong, H. Zhang, W. Wang, L. Colombo, R. M. Wallace and K. Cho, *Appl. Phys. Lett.*, 2013, **103**, 053513.
26 S. McDonnell, R. Addou, C. Buie, R. M. Wallace and C. L. Hinkle, *ACS Nano*, 2014, **8**, 2880–2888.
27 H.-Y. Chang, W. Zhu and D. Akinwande, *Appl. Phys. Lett.*, 2014, **104**, 113504.
28 B. Radisavljevic, A. Radenovic, J. Brivio, V. Giacometti and A. Kis, *Nat. Nanotechnol.*, 2011, **6**, 147–150.
29 W. Shi, L. Huo, H. Wang, H. Zhang, J. Yang and P. Wei, *Nanotechnology*, 2006, **17**, 2918.
30 T. Kim, D. Kang, Y. Lee, S. Hong, H. G. Shin, H. Bae, Y. Yi, K. Kim and S. Im, *Adv. Funct. Mater.*, 2020, **30**, 2004140.
31 W. Zhu, X. Wei, F. Yan, Q. Lv, C. Hu and K. Wang, *J. Semicond.*, 2019, **40**, 092001.
32 X. Wei, F. Yan, Q. Lv, W. Zhu, C. Hu, A. Patanè and K. Wang, *Adv. Opt. Mater.*, 2019, **7**, 1900190.

33 Q. Lv, F. Yan, X. Wei and K. Wang, *Adv. Opt. Mater.*, 2018, **6**, 1700490.
34 F. Yan, Z. Wei, X. Wei, Q. Lv, W. Zhu and K. Wang, *Small Methods*, 2018, **2**, 1700349.
35 B. Radisavljevic, M. B. Whitwick and A. Kis, *ACS Nano*, 2011, **5**, 9934–9938.
36 Z. Jiang, C. Wang, G. Du, Y. Zhong and J. Jiang, *J. Mater. Chem.*, 2012, **22**, 9494–9496.
37 L. Liu, N. Xu, Y. Zhang, P. Zhao, H. Chen and S. Deng, *Adv. Funct. Mater.*, 2019, **29**, 1807893.
38 A. M. Afzal, Y. Javed, N. A. Shad, M. Z. Iqbal, G. Dastgeer, M. M. Sajid and S. Mumtaz, *Nanoscale*, 2020, **12**, 3455–3468.
39 W. Yan, O. Txoperena, R. Llopis, H. Dery, L. E. Hueso and F. Casanova, *Nat. Commun.*, 2016, **7**, 1–6.
40 Y. Sun, H. Cheng, S. Gao, Z. Sun, Q. Liu, Q. Liu, F. Lei, T. Yao, J. He and S. Wei, *Angew. Chem., Int. Ed.*, 2012, **51**, 8727–8731.
41 A. M. Afzal, G. Dastgeer, M. Z. Iqbal, P. Gautam and M. M. Faisal, *ACS Appl. Mater. Interfaces*, 2020, **12**, 19625–19634.
42 D. S. Schulman, A. J. Arnold and S. Das, *Chem. Soc. Rev.*, 2018, **47**, 3037–3058.
43 Y. Mao, C. Xu, J. Yuan and H. Zhao, *J. Mater. Chem. A*, 2019, **7**, 11265–11271.
44 X.-R. Nie, B.-Q. Sun, H. Zhu, M. Zhang, D.-H. Zhao, L. Chen, Q.-Q. Sun and D. W. Zhang, *ACS Appl. Mater. Interfaces*, 2017, **9**, 26996–27003.
45 K. Xu, Y. Huang, B. Chen, Y. Xia, W. Lei, Z. Wang, Q. Wang, F. Wang, L. Yin and J. He, *Small*, 2016, **12**, 3106–3111.
46 Y. Ke, D. Qi, C. Han, J. Liu, J. Zhu, Y. Xiang and W. Zhang, *ACS Appl. Electron. Mater.*, 2020, **2**, 920–926.
47 S. Fathipour, N. Ma, W. Hwang, V. Protasenko, S. Vishwanath, H. Xing, H. Xu, D. Jena, J. Appenzeller and A. Seabaugh, *Appl. Phys. Lett.*, 2014, **105**, 192101.
48 T. Kanazawa, T. Amemiya, A. Ishikawa, V. Upadhyaya, K. Tsuruta, T. Tanaka and Y. Miyamoto, *Sci. Rep.*, 2016, **6**, 22277.
49 Y. Wang, J. C. Kim, R. J. Wu, J. Martinez, X. Song, J. Yang, F. Zhao, A. Mkhoyan, H. Y. Jeong and M. Chhowalla, *Nature*, 2019, **568**, 70–74.
50 F. A. Rasmussen and K. S. Thygesen, *J. Phys. Chem. C*, 2015, **119**, 13169–13183.
51 J. Shang, S. Zhang, X. Cheng, Z. Wei and J. Li, *RSC Adv.*, 2017, **7**, 14625–14630.
52 J. Shim, S. Oh, D.-H. Kang, S.-H. Jo, M. H. Ali, W.-Y. Choi, K. Heo, J. Jeon, S. Lee, M. Kim, Y. J. Song and J.-H. Park, *Nat. Commun.*, 2016, **7**, 13413.
53 A. M. Afzal, M. Z. Iqbal, S. Mumtaz and I. Akhtar, *J. Mater. Chem. C*, 2020, **8**, 4743–4753.
54 A. M. Afzal, M. Z. Iqbal, G. Dastgeer, G. Nazir, S. Mumtaz, M. Usman and J. Eom, *ACS Appl. Mater. Interfaces*, 2020, **12**, 39524–39532.
55 A. M. Afzal, S. Mumtaz, M. Z. Iqbal, M. W. Iqbal, A. Manzoor, G. Dastgeer, M. J. Iqbal, Y. Javed, R. Khan, N. A. Shad, M. M. Sajid and T. Zahid, *J. Mater. Chem. C*, 2021, **9**, 7110–7118.
56 G. Dastgeer, A. M. Afzal, G. Nazir and N. Sarwar, *Adv. Mater. Interfaces*, 2021, **8**, 2100705.
57 L. Britnell, R. V. Gorbachev, A. K. Geim, L. A. Ponomarenko, A. Mishchenko, M. T. Greenaway, T. M. Fromhold, K. S. Novoselov and L. Eaves, *Nat. Commun.*, 2013, **4**, 1794.
58 A. Mishchenko, J. S. Tu, Y. Cao, R. V. Gorbachev, J. R. Wallbank, M. T. Greenaway, V. E. Morozov, S. V. Morozov, M. J. Zhu, S. L. Wong, F. Withers, C. R. Woods, Y. J. Kim, K. Watanabe, T. Taniguchi, E. E. Vdovin, O. Makarovsky, T. M. Fromhold, V. I. Fal'ko, A. K. Geim, L. Eaves and K. S. Novoselov, *Nat. Nanotechnol.*, 2014, **9**, 808–813.
59 M. P. Mikhailova, K. D. Moiseev and Y. P. Yakovlev, *Semicond. Sci. Technol.*, 2004, **19**, R109–R128.
60 M. Mikhailova, K. Moiseev and Y. P. Yakovlev, *Semicond. Sci. Technol.*, 2004, **19**, R109.
61 V. L. Rideout, *Thin Solid Films*, 1978, **48**, 261–291.
62 P. Zhou, J. Cheng, C. F. Schaus, S. Z. Sun, K. Zheng, E. Armour, C. Hains, W. Hsin, D. R. Myers and G. A. Vawter, *IEEE Photonics Technol. Lett.*, 1991, **3**, 591–593.